Ceramics International 48 (2022) 31191–31202

Contents lists available at ScienceDirect

Ceramics International

journal homepage: www.elsevier.com/locate/ceramint

Solvothermal synthesis and characterization of ytterbium/iron mixed oxide nanoparticles with potential functionalities for applications as multiplatform contrast agent in medical image techniques

M.P. Yeste [a,b], C. Fernández-Ponce [c,d], E. Félix [b,f], M. Tinoco [e], R. Fernández-Cisnal [c,d], C. García-Villar [d,i], C. Pfaff [g], J. Kriwet [g], E. Natividad [h], M.A. Cauqui [a,b], F. Garcia-Cozar [c,d], R. Litrán [b,f,*], O. Bomati-Miguel [b,f]

[a] Department of Materials Science and Metallurgic Engineering, and Inorganic Chemistry, Faculty of Sciences, University of Cádiz, Puerto Real, 11510 Cádiz, Spain
[b] IMEYMAT: Institute of Research on Electron Microscopy and Materials of the University of Cádiz, Puerto Real, 11510, Cádiz, Spain
[c] Department of Biomedicine, Biotechnology and Public Health, University of Cadiz, Spain
[d] Institute of Biomedical Research Cádiz (INIBICA), Cadiz, Spain
[e] ICTS – Centro Nacional de Microscopía Electrónica, Universidad Complutense de Madrid, 28040, Madrid, Spain
[f] Department of Condensed Matter Physics, Faculty of Sciences, University of Cádiz, Puerto Real, 11510, Cádiz, Spain
[g] University of Vienna, Faculty of Earth Sciences, Geography and Astronomy, Department ofPalaeontology, 1090, Vienna, Austria
[h] Instituto de Nanociencia y Materiales de Aragón (INMA), CSIC-Universidad de Zaragoza, EINA. Edificio Torres Quevedo, María de Luna, 3, 50018, Zaragoza, Spain
[i] Radiology Department, Hospital Universitario Puerta del Mar. Ana de Viya Avenue, n 21.11009, Cádiz, Spain

ARTICLE INFO

Keywords:
Ytterbium-iron nanoparticles
Functionalization
Multiplatform contrast agents
Solvothermal process
CT
MRI

ABSTRACT

A solvothermal route to prepare Glutathione capped hybrid ytterbium/iron oxide nanoparticles with potential applications as multiplatform contrast agent in medical image techniques has been developed. The influence of ytterbium/iron molar ratio used as precursor, as well as the degree of the autoclave filling on the structural and morphological characteristics of the obtained nanoparticles has been extensively studied. Although all nanoparticles present similar composition, with $YbFeO_3$ being the majority phase, size and morphology of the as synthetized nanoparticles are highly influenced by the critical temperature and by the over -saturation reached during the solvothermal process. We have demonstrated that glutathione properly functionalizes the hybrid nanoparticles, increasing their colloidal stability and decreasing their cytotoxicity. Additionally, they show good imaging in magnetic resonance and X-ray computerized tomography, thereby indicating promising potential as a dual contrast agent. This work presents, for the first time, glutathione functionalized ytterbium/iron oxide nanoparticles with potential applications in Biomedicine.

1. Introduction

Non-invasive imaging techniques are fundamental tools in medicine for early detection and screening for severe pathologies [1–3]. Together with nuclear medicine imaging techniques, Magnetic Resonance Imaging (MRI) and X-ray computerized tomography (CT) are the most employed, because they provide anatomical and functional information from inside the body [4]. However, in order to enhance image contrast to distinguish soft tissues and to provide additional functional information, contrast agents (CA) have to be used [5,6]. The most frequently used CA are iodate systems and Gd^{3+} chelates for CT [7] and MRI [8] respectively. However, these molecular contrast agents present several limitations: i) only a small part of them generate contrast; ii) they have low specificity for the detection of non-vascularized tissues, including tumors [6]; iii) they can cause adverse effects due to their toxicity and rapid kidney excretion [9] and iv) in the case of iodinated compounds used for CT, they have low efficiency because their K-edge energy coefficient (33 KeV) is outside voltage ranges used in medicine. Recent advances on the synthesis, characterization and surface functionalization of nanoparticles (NPs), have provided an interesting alternative to these conventional CA [10,11]. In this sense, different NP systems have been proposed as imaging probes, with some of them already being used as commercial contrast agents or even in preclinical studies [12,13]. Magnetic NPs can be used as MRI CA, and radio opaque NPs, including

* Corresponding author. Institute of Research on Electron Microscopy and Materials of the University of Cádiz, Puerto Real, 11510, Cádiz, Spain.
E-mail addresses: curro.garcia@uca.es (F. Garcia-Cozar), rocio.litran@uca.es (R. Litrán).

https://doi.org/10.1016/j.ceramint.2022.06.194
Received 8 April 2022; Received in revised form 2 June 2022; Accepted 17 June 2022
Available online 26 June 2022

several metallic and metal oxides NPs, have been proposed for CT CA [14–16].

Iron oxide magnetic phases, especially maghemite (Fe_2O_3), and magnetite (Fe_3O_4) have been used as CA for MRI [17–20]. On the other hand, gold NPs were the first type of NPs used for CT CA [21]. However, less expensive alternatives have been explored. Many NPs comprised of heavy elements with high atomic number (high- Z) are proposed as a new class of CT contrast media to address shortcomings attributed to clinical iodinated agents. Over the range of 100–140 kVp, which are feasible settings for CT, barium, gadolinium, ytterbium, and tantalum produce higher CT image contrast than that achieved by currently available iodinated contrast agents at equal mass concentration [22–25].

Nevertheless, combination of different imaging techniques is usually required to accomplish accurate diagnoses. Thus, the possibility to obtaining a multiplatform CA that can simultaneously be used in MRI and CT, can contribute to obtaining complementary information provided by both imaging techniques. A growing effort has been carried out for the fabrication of hybrid NPs than can be used as multiplatform CA for medical imaging [26].

Ytterbium ferrite hybrid NPs can be appropriate candidates for multiplatform CA for medical imaging [25]. These hybrid NPs can be synthetized by different bottom up methods such as co-precipitation, thermal decomposition, microwave or solvothermal synthesis [27,28]. In the latter, the reaction takes place at higher than atmospheric pressure and at temperatures higher than the solvent boiling point, originating supercritical conditions for the reaction. Synthesis of metal oxide and mixed oxide NPs by solvothermal method has been actively investigated. One of the advantages of the solvothermal method is that it allows for the formation of mixed oxides without calcination making this synthetic method an interesting alternative for the preparation of hybrid metal oxide NPs for multiplatform CA in medical imaging. Additionally, rare-earth-activated systems have been extensively studied due to their excellent photoluminescent properties, especially in up conversion emission [29]. These systems based on rare-earth-doped, can be employed in optical bioimaging. Yb^{3+} ions are exceptional luminescence sensitizers for other rare earth ions, due to their effective absorption cross section at 980 nm [30].

Moreover, NPs used for biomedical applications have to achieve some fundamental requisites: low cytotoxicity, colloidal stability, and availability for subsequent bioconjugatin with other biomolecules. Surface functionalization is a common strategy, not only to subsequently promote crosslinking between NPs and specific biological species, but also to minimize NP cytotoxicity and unspecific binding to biological structures [31]. Functionalization of the NP surface with species containing bio-active terminal groups, such as amino or carboxylic groups, allows for subsequent linking to relevant biomolecules needed for targeted applications [32,33]. NP functionalization can also contribute to avoiding aggregation, minimizing accumulation in organs and/or phagocyte activation, thus maintaining a prolonged circulation time [34].

In this work, we have developed a one pot route to synthetize ytterbium ferrite hybrid oxide NPs by a solvothermal reaction at 300 °C, based on the previous works by Hosokawa et al. [35,36], using 1,4-butanediol as organic solvent and 1,6 hexanediamine as capping agent, contributing to control nanocrystal growth and decreasing its aggregation. We have synthetized different hybrid ytterbium iron oxide systems, following a solvothermal route and changing two synthesis parameters: the degree of autoclave filling and the ytterbium/iron precursor ratio. By changing the level of autoclave filling, we modify the autogenous pressure of the solvothermal process as well as the time required to get critical temperature, which can influence NP structural characteristics. Additionally, we have used different molar iron/ytterbium precursor ratios, analyzing the final iron/ytterbium ratio in the formed NPs, a highly relevant parameter for efficient multiplatform CA NPs. We have carried out the solvothermal process in the presence of 1, 6-hexanediamine, in order to control NP growth and to get NPs with narrower size distribution. Subsequently, by a ligand exchange process, and with the aim to obtaining biocompatible NPs, we have performed the "ex situ" functionalization of mixed oxide NPs, using glutathione (GSH) as capping molecule, and replacing the initial hexanediamine used to stabilize NPs during synthesis. GSH as capping agent is a tripeptide containing a thiol, two carboxylic and an amine terminal groups, that are available for the functionalization of mixed oxide NPs [37–39]. We have combined electron microscopy-based structural and compositional nanoanalyses to obtain information about NP composition, in order to confirm the formation of hybrid oxide NPs conformed by a mixed ytterbium/iron oxide, characteristic of crucial interest for biomedical applications as multiplatform contrast agent in medical imaging. This characterization will also allow us to know whether GSH has properly been linked to the NP surface, functionalizing it. We have studied the colloidal stability of functionalized NPs comparing them to those without GSH capping. We have used Fourier Transform Infrared spectroscopy to study the linkage mechanism by which GSH is bonded to the NP surface, to ascertaining GSH functional groups available for the subsequent crosslinking processes.

In order to study potential applications in optical imaging, we have also analyzed optical absorption and emission of these NPs. Although the emission properties of these systems are extremely enhanced due to energy transfer processes induced by interactions between different rare-earth cations, the Yb^{3+} ions forming part of the ytterbium/iron oxide NPs studied in this work, can also induce interactions that contribute to their emission.

Finally, we have studied the biocompatibility as well as the efficiency of our NPs as MRI/CT CA. Cytotoxicity has been studied analyzing cells viability after incubation with different NP concentrations, in order to obtain information about NP biocompatibility. In order to evaluate the potential use of NPs as CA, phantoms with different NP concentrations have been prepared and scanned in a clinical grade MRI and CT. The results demonstrated that Fe/Yb NPs showed favorable biocompatibility and good signals for dual MR/CT contrast imaging. Thus, the main objective of our work is to deepen in the knowledge of the synthesis and characteristics of the ytterbium/iron oxide NPs, their functionalization with GSH, and the biocompatibility of the resultant NP-based system, providing the base for a product that could be successfully utilized as CA for medical imaging techniques.

2. Experimental

2.1. Chemicals

Iron acetylacetonate ($Fe(C_5H_7O_2)_3$ (Fe(acac)3)), ytterbium chloride ($YbCl_3.6H_2O$), 1,4-bytanediol ($C_4H_{10}O_2$), 1,6-hexanediamine ($C_6H_{16}N_2$) and reduced glutathione ($C_{10}H_{17}N_3O_6S$, GSH) were all purchased from Sigma-Aldrich and used without further purification.

2.2. Iron/ytterbium mixed oxide NPs synthesis

NPs have been synthetized using a solvothermal method based on the reactions reported by Hosokawa et al. [36]. We have modified this procedure, changing diverse reaction parameters, such as, the reactor filling, the ytterbium precursor and the starting precursor concentration, in order to achieve a higher monodispersity and to reduce NP aggregation. Firstly, 10.44 g of 1,6-hexanediamine used as surfactant, were solved in 70 mL of 1,4-butanediol used as solvent for the solvothermal reaction due to its high boiling point (235 °C). In a standard preparation, 0.53 g of $Fe(acet)_3$ were then solved in this mixture. With the aim to study the influence of Yb/Fe ratio on the final chemical composition of the resulting NPs, $YbCl_3$ was added in concentrations such as to get molar Yb/Fe precursor ratios of 2, 1, 0.6, 0.3 and 0.05.

The mixture was placed in a Teflon reactor for a 200 mL autoclave. With the aim of studying the influence of the degree of autoclave filling

and consequently, the autogenous pressure value on NP characteristics, the reaction was carried out filling the reactor at two different levels (specifically, at 80% and 66% of its total capacity). This parameter determines the critical temperature of the solvothermal process, the reaction time and consequently, precursors supersaturation during the reaction. The autoclave was purged with nitrogen and heated at 300 °C at a rate of 2.3 °C/min without stirring. After 2 h the reaction was stopped and the obtained product was washed three times with ethanol, centrifuged and air dried.

Obtained NPs were coded by Yb-FeX, where X indicates Yb/Fe precursor molar ratio. X values of 2, 1, 0.6, 0.3 or 0.05 have been used. In the cases of reactions performed at lower autogenous pressure (reactor filling at 66% of the total capacity), the code L is added. Table 1 summarizes the different types of NPs prepared.

2.3. Functionalization of iron/ytterbium mixed oxide NPs

Functionalization has been performed using GSH as capping molecule. This process takes place by a ligand exchange reaction in which the hexanediamine used as surfactant in the NP synthesis is replaced by GSH, which binds to the NP surface. Briefly, 25 mg of Yb-FeX and 50 mg of GSH [37,39] were solved in 10 mL Milli Q water and sonicated in an ultrasonic bath during 30 min. After this time, the solution was placed in an orbital shaker and stirred during 8 h. After this process, resulting NPs were washed three times and filtered with a mixture of ethanol and water to eliminate non-linked GSH as well as the remaining hexanediamine.

Fig. 1 shows a diagram of the synthetic process.

2.4. Characterization

2.4.1. Structural and compositional characterization

Structure and chemical composition of the NPs were first analyzed. Firstly, the crystalline structure of the as-synthesized NPs was studied by X-Ray Powder Diffraction (XRD) in a Bruker D8 Advance diffractometer using CuKα radiation in the 15-65° angular range. Identification of the different crystalline phases present in these NPs was performed by the DIFFRAC.EVA V.3.0 software from Bruker AXS and Inorganic Material Database (AtomWork) from the National Institute for Materials Science and Materials Phases Data System.

Structural and compositional characterization of all samples has also been performed using different Transmission Electron Microscopy (TEM) related techniques. Imaging techniques such as conventional TEM, High Resolution Transmission Electron Microscopy (HRTEM) and High-Angle Annular Dark Field Scanning Transmission Electron Microscopy (HAADF-STEM) allowed us to visualize structural features, such as NP size or atomic structures. On the other hand, energy dispersive X-ray spectrometry (EDX) has been used to collect the atomic composition on specific areas, as well as to draw compositional maps of areas ranging from few nm^2 up to μm^2. TEM analyses were carried out in a Talos F200X, operating at a 200 kV accelerating voltage. Samples were prepared by depositing 10 μL of NP colloidal solution, which were drop-casted onto a holey-carbon coated Cu grid and dried for 5 h. EDX spectra were collected using a Super X G2 XEDS system and analyzed by Velox software. For obtaining the size distributions, around 200 NPs were counted from the TEM images, using the Image J software. In the case of particles with rod-like structures, the width of the particles was measured. In addition, we obtained the average particle size and the standard deviation [40–42].

Table 1
Synthetized NPs, as a function of Yb/Fe molar ratio and degree of autoclave filling, as well as codes assigned to each type of NP.

NPs code	Yb/Fe molar ratio	Degree of autoclave filling (%)
Yb-Fe2	2	80
Yb-Fe1	1	80
Yb-Fe0.6	0.6	80
Yb-Fe0.3	0.3	80
Yb-Fe0.05	0.05	80
Yb–Fe2L	2	66
Yb–Fe1L	1	66

2.4.2. Colloidal stability and functionalization characterization

In order to study the colloidal stability of NPs before and after the GSH functionalization process, size distribution and zeta potential in ultrapure water (MQ) were studied. Measurements were performed using Dynamic Light Scattering; DLS (Zetasizer Nano ZS90, Malvern Instruments, equipped with software version 7.10) at 1 mg L^{-1}. The NP colloidal dispersions were transferred to a 1.5 ml square cuvette for DLS measurements, performed at 20 °C with samples equilibrated for 2 min before the measurements were started. Fifteen consecutive measurements were collected and averaged to calculate the mean size. The polydispersity index (PDI) was calculated to estimate the size dispersion in samples.

Fourier-transform infrared spectroscopy (FTIR) was used to obtain information about the linking between GSH and the NP surface. Experiments were recorded with a Bruker Alpha System Spectrophotometer (KBr wafer technique), using the same quantity of sample in all measurements.

2.4.3. Optical characterization

Absorption spectra were acquired with a Lambda 19 PerkinElmer spectrophotometer ("PerkinElmer", MA, U.S.A.).

2.4.4. X-ray attenuation measurements

To measure the X-ray absorption capacity of the as synthesized Yb–Fe Nps, a cylindrical preforms sample (2 mm in height and 0.8 mm in diameter) were obtained via a biaxial pressing of dried Yb–Fe NPs powder. The X-ray absorption was investigated by using a Skyscan/Bruker Micro-CT Device 1173. In these experiments, the sample preforms were irradiated with X-ray generated by a tungsten tube working at 90 KV.

2.4.5. Cytotoxicity assay and cell culture

Jurkat cells (American Type Culture Collection, Manassas, VA, USA) were cultured at 37°C, in a 5% CO_2 atmosphere, in Dulbecco's Modified Eagle's Medium (DMEM) containing 2 mM L-glutamine, 10 mM Hepes, 10% (v/v) heat-inactivated fetal bovine serum (FBS), 1% (v/v) non-essential amino acids (NEAA), 1% (v/v) sodium pyruvate, 50 μM 2-mercaptoethanol, 100 U/ml penicillin and 100 μg/ml streptomycin (all from Life Technologies, Carlsbad, CA, USA).

2.4.6. Cytotoxicity and cell viability

Jurkat cells, $5x10^5$ cells were cultured in a 48 well plate, in the absence or presence of nanoparticles at 1.5 μg/ml or 15 μg/ml.

Cell viability was analyzed 24 h after addition of NPs by an MTT-based assay as previously described [43]. Briefly, MTT reactant (Thiazolyl Blue Tetrazolium Bromide, TOX1-1 KT, Sigma Aldrich) was added to the cells in a 1:10 ratio (MTT solution/culture medium) and incubated during 3 h at 37°C. Then, formazan crystals formed inside the cells were dissolved by adding MTT Solubilization Solution (M – 8910, Sigma Aldrich) at 1:2 with vigorous pipetting. Optical density at 570 nm was evaluated to quantify the amount of formazan crystals, which is proportional to the number of viable cells (background absorbance was measured at 690 nm and subtracted from the 570 nm measurement). Viability was compared to untreated controls (100%)). Media in the absence of cells was used as blank; while cells, cultured in the presence of 10% dimethyl sulfoxide (DMSO), was used as control for decreased cell viability, being always below 10%. Statistical analysis was performed using the Statgraphics software. Significance was determined using ANOVA and Multiple Range Tests.

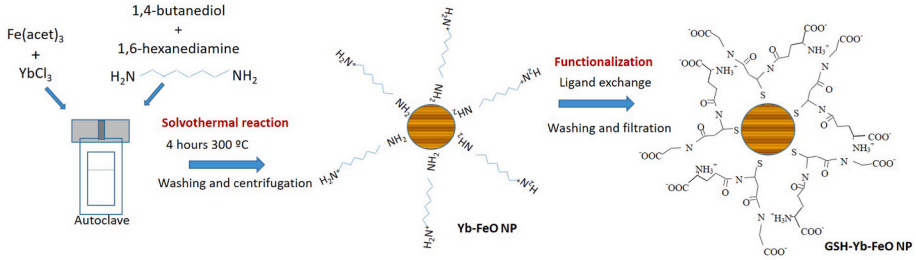

Fig. 1. Synthesis procedure outline.

2.4.7. CT and MRI in vitro measurements

In order to perform in vitro MRI/CT measurements, phantoms were prepared in a suite of 1.5 mL tubes. 50uL of NPs in deionized water at concentrations of: 20 mg/mL, 15 mg/mL, 10 mg/mL, 5 mg/mL and 2.5 mg/mL; were dispersed by a 10 min' incubation in an ultrasound water bath (FisherBrand F15052, 140W). Subsequently, 1 mL of a solution containing 30% acrylamide/Bisacrylamide 37.5:1 and 0,5% Ammonium Persulfate, was added. Samples were vigorously vortexed and 10uL TEMED (tetramethylethylenediamine) was immediately added to cause a fast gelification of acrylamide/Bisacrylamide.

T2-weigted MRI was performed in vitro using an inversion recovery pulse sequence (Siemens MAGNETOM Tim MRI scanner) at 1.5 T. The experimental conditions were performed using a recycle time (TR) of 3500 ms, and a field of view (FOV) of 100 × 100 cm^2. As well, in vitro CT images were acquired using a Revolution EVO EX (General Electric Healthcare).

3. Results

3.1. Effect of ytterbium/iron ratio

Fig. 2 displays XRD powder diffractograms of Yb–Fe NPs synthesized using the same autoclave filling volumes (80%), but varying the molar Yb/Fe precursor ratio from 0.05 to 2. In addition, Table SI (supplementary information) shows experimental values of the recorded XRD peaks, 2θ degrees, and the corresponding Miller indices (hkl) indexation. On the one hand, XRD powder diffractogram recorded for Yb–Fe NPs, which were synthesized using Yb/Fe precursor molar ratios equal to or greater than 1, display a battery of well-defined peaks, which correspond mainly to an orthorhombic (space group *P*nma) ytterbium ferrite phase type $YbFeO_3$ and to a lesser extent to a trigonal (Rhombohedral space group R3 ¯m) ytterbium ferrite phase type YbFe2O4) [44]. In addition, six small peaks have been identified in this diffractogram, which could be assigned to the crystalline planes of a hexagonal (non-polar *P*63/mmc or polar *P*63cm) polymorph of an $YbFeO_3$ phase (peak sited at 56.5 2-theta degrees). It is a well-known fact that, although, bulk $YbFeO_3$ showed an orthorhombic perovskite structure (Pbnm/Pnma), in the nanometer size range, $YbFeO_3$ can take two metastable hexagonal phases (non-polar *P*63/mmc and polar *P*63cm), which are dependent on oxygen partial pressure [45]; therefore, the presence of small amounts of this hexagonal phase, either in the form of isolated nanoparticles or as small crystals included within the orthorhombic YbFeO3 NPs, cannot be excluded. Table 2 shows the percentages of each of the mineral phases present in sample Yb-Fe1 obtained from the analysis of their XRD powder diffractogram by using the software DIFFRAC.EVA.V3.0.

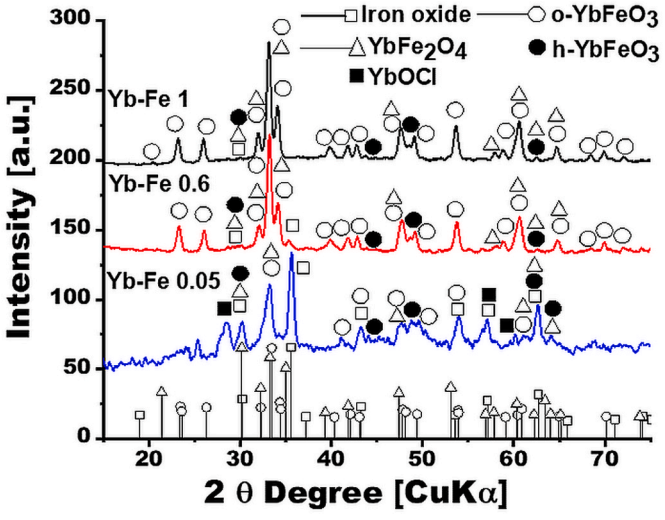

Fig. 2. XRD powder diffractograms recorded for Yb–Fe NPs samples synthesized at 80% autoclave filling volume, by changing the starting ytterbium/iron molar precursor ratio.

On the other hand, XRD powder diffractogram of the YB-Fe NPs samples synthesized using a Yb/Fe precursor molar ratios equal to or lower than 0.6 showed, approximately, the same battery of peaks attributed to an orthorhombic or/and hexagonal $YbFeO_3$ phase, and a trigonal $YbFe_2O_4$ phase, which had been described above for the Yb-Fe1 NPs. However, in this case, two low intensity peaks were also observed near 30.2 and 35.4 2-theta (degrees), which could be ascribed mainly to crystalline planes of a cubic (space group Fd-3m) inverse spinel structure either magnetite (Fe_3O_4) (International Centre for Diffraction Data. Powder Diffraction FileTM (PDF®) 2018–2019, file JCPDS 89–0691. Http://www.icdd.com: 2018) or maghemite (γ-Fe2O3) [46]. Thus, the analysis of these diffractogram suggested that samples, which were synthesized by using a Yb/Fe precursor molar ratios equal or lower than 0.6, were formed mainly by ytterbium ferrite NPs with a very small fraction of iron oxide nanocrystals, either in the form of small NPs or arranged on the ytterbium ferrite NPs surface. The percentages of the different mineral phases present in samples Yb-Fe0.6 is listed in Table 2. It is important to point out that the amount of the iron oxide phase present in the samples increases as the amount of ytterbium precursor used in its synthesis decreases. This is very well observed in the case of diffractograms recorded for the sample synthesized by using an Yb/Fe precursor molar ratio of 0.05, which reveals the presence of six very intense and well-defined peaks, corresponding to a cubic (space group Fd-3m) iron oxide phase (either maghemite or magnetite) which stand out on a battery of small peaks attributed to a trigonal $YbFe_2O_4$ phase or

Table 2
Percentages of mineral phases present in each sample estimated by using the software DIFFRAC.EVA.V3.0

Sample	$YbFeO_3$-o [%]	$YbFeO_3$-h [%]	$YbFe_2O_4$ [%]	Iron oxide [%]	YbOCl [%]
Yb-Fe0.05	**30**	**5**	**12**	**53**	**0**
Yb-Fe0.6	**75**	**9**	**11**	**5**	**0**
Yb-Fe1	**80**	**10**	**10**	**0**	**0**
Yb–Fe1L	**62**	**10**	**20**	**5**	**3**
Yb–Fe2L	**59**	**8**	**16**	**7**	**10**

to an orthorhombic or/and hexagonal YbFeO3 phase. The mineral phase percentage analysis of this diffractogram by using DIFFRAC.EVA.V3.0 (see Table 2) revealed an iron oxide content of more than 50%; which suggests that this sample is composed of a mixture of iron oxide nanoparticles and ytterbium ferrite nanoparticles. Finally, it is important to point out the presence in this last diffractogram of three small peaks corresponding to an intermediate rhombohedral (space group R-3m) YbOCl phase (International Centre for Diffraction Data. Powder Diffraction FileTM (PDF®) 2003, file JCPDS 49–1802. http://www.icdd.com). The presence of this phase, formed as an intermediate of the reaction, indicates a lower efficiency of this synthesis conditions to promote the complete union between iron and ytterbium atoms dissolved in the synthesis medium.

General views of Yb–Fe NPs prepared using different ytterbium/iron ratios and prepared with the same degree of autoclave filling, are shown in Fig. 3, where representative TEM micrographs of these NPs are presented, as well as their corresponding particle size distributions, fitted to Gaussian functions, obtained from the analyses of more than 200 NPs. Fig. 3 displays TEM micrographs for Yb-Fe2 (a), Yb-Fe1 (b), Yb-Fe0.6 (c), Yb-Fe0.3 (d) and Yb-Fe0.05 (e). The autogenous pressure of the reaction has been kept constant by controlling the filling of the hydrothermal reactor (80% of the total volume for all samples compared in this figure). Micrographs corresponding to NPs prepared with ytterbium/iron molar ratios equal to or higher than 1 (Fig. 3a and 3 b), reveal the formation of NPs with cuboctahedral morphology and average sizes between 50 and 60 nm for Yb-Fe2 and around 35 nm for Yb-Fe1, showing these last NPs a narrower size distribution. We have to take into account that the cuboctahedral morphology is indicative of a high

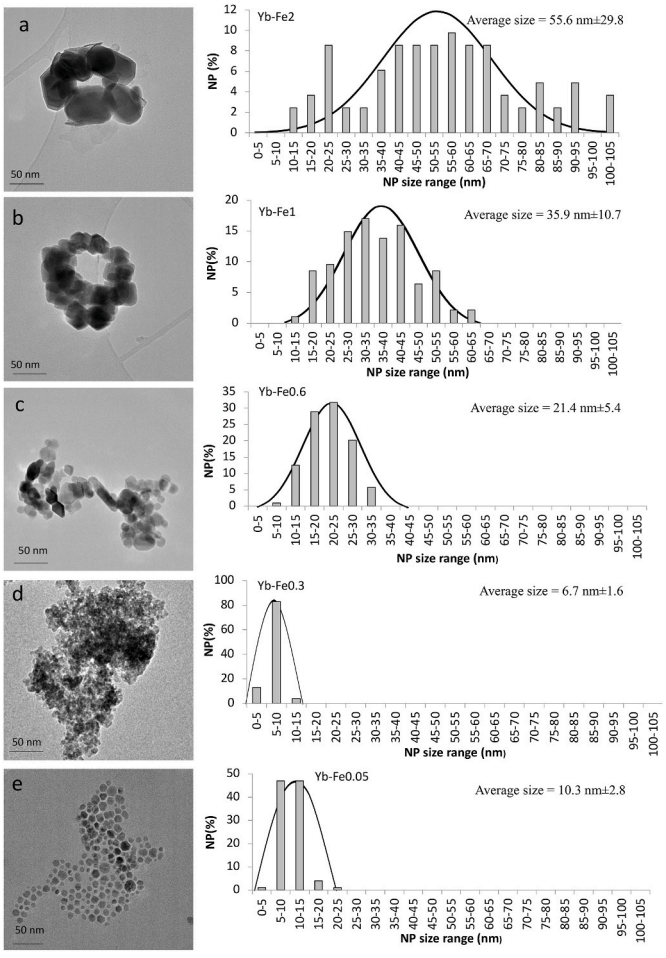

Fig. 3. TEM micrographs and their corresponding NP size distributions for Yb–Fe NPs prepared varying the starting ytterbium/iron molar ratio.

degree of symmetry. These NPs have been prepared with a high percentage of autoclave filling (80%). Under these conditions, the critical temperature value decreases and the precursor super-saturation increases, inducing a fast nucleation and probably the formation of morphologies with a high degree of symmetry. Some evidences of aggregation are found in both cases, and most probably magnetic interactions between these NPs play a role in this attachment. However, this aggregation induces a particular circle-assembly in the case of NPs prepared with an ytterbium/iron ratio of 1. The shape factor and the faceted morphology of these NPs is surely a relevant factor for this arrangement. This conformation does not appear for other ytterbium/iron proportions, evidencing the starting iron proportion influence on the NPs magnetic behavior and consequently on the NPs conformation. Changes in NP morphology are revealed when the solvothermal reaction is carried out using molar ytterbium/iron ratios lower than 1. The micrograph corresponding to Yb-Fe0.6 NPs (Fig. 3c) reveals formation of smaller NPs and interestingly, presence of some nano-rods. In this case, the process is developed with a lower ytterbium concentration and the reaction critical conditions induced by the high degree of reactor filling is not enough to generate the high over-saturation needed for a fast nucleation, as it was observed for higher ytterbium proportions. Therefore, cRod-like structures, with a lower degree of symmetry are obtained. In the case of Yb-Fe0.3 (Fig. 3d), the image shows the formation of small NPs immersed in an amorphous cloud. Probably in this case, the amount of ytterbium is not enough for the formation of the mixed oxide and different ytterbium compounds and thus, ytterbium chlorates are formed, surrounding the hybrid NPs. When the ytterbium precursor concentration is extremely low, as in the case of Yb-Fe0.05 (Fig. 3e), the TEM image shows the formation of homogeneous and well distributed small NPs but probably, with a composition without a detectable fraction of ytterbium. In general, we observe a clear influence of ytterbium precursor molar concentration on NP morphology and size. Summarizing, ytterbium/iron molar fractions equals or higher that 1, yield cuboctahedral NPs while less symmetrical structures are formed when the ytterbium/iron ratio decreases to 0.6. Finally, smaller NPs are obtained from syntheses with lower ytterbium/iron ratios. It has been reported that $YbFeO_3$ nucleation frequency decreases by the presence of chloride ions in the solvothermal reaction system [35,36]. Considering that the ytterbium precursor used was ytterbium chloride, this may explain the smaller average NP size for lower ytterbium/iron ratios. Additionally, and considering that NPs are formed by nucleation and growing processes, the excess of ytterbium solved in the media, together with the excess of iron, could contribute to an increase in the average size of mixed oxide NP by Ostwald ripening mechanism.

In order to deepen in the analysis of the influence of ytterbium/iron ratios on NP crystal structure, HRTEM images of representative NPs prepared with different ytterbium/iron ratios and with the same level of autoclave filling were performed and are shown in Fig. 4. On the one hand, Digital Diffraction Patterns (DDPs) displayed in Fig. 4 clearly point out that o-$YbFeO_3$ mixed oxide was identified in quite large quantities in the four samples with higher concentration of Yb (Fig. 4a–d), while interplanar distances corresponding to the planes of trigonal $YbFe_2O_4$ phase in these DDPs were not observed. This agrees with results obtained by XRD analysis. In particular, HRTEM images of $YbFeO_3$ crystals closely oriented along the [010] zone axis were acquired for several of these samples. For example, in sample Yb-FeO2 (Fig. 4a), {004} $YbFeO_3$ reflections, with atomic distances of 1.9 Å were observed, forming 70° and 44° with diffraction spots at 2.5 and 1.8 Å, characteristic of {20–1} and {203} $YbFeO_3$ planes respectively. Similarly, in sample Yb-Fe1 (Fig. 4b), the same {004} and {203} $YbFeO_3$ reflections were observed, but in this case another $YbFeO_3$ diffraction spot was visible: {20–2} with an atomic distance of 2.2 Å, generating 55° and 11° angles with respect to {004} and {203} lattice planes respectively. A {004} $YbFeO_3$ spot is also seen in the crystal analyzed on Fig. 4 d (sample Yb-Fe0.3), which is also oriented along the [010] zone axis. This diffraction spot forms a 90° angle with a reflection whose distance

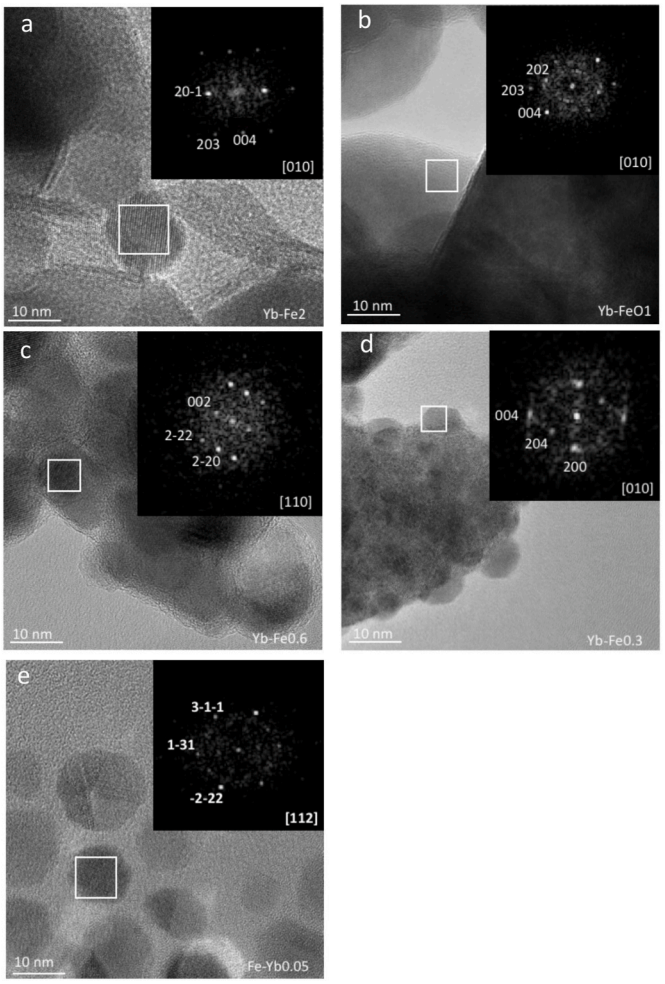

Fig. 4. HRTEM images of Yb–Fe NPs prepared varying the starting ytterbium/iron molar ratio.

is 2.6 Å, which corresponds to $YbFeO_3$ {200} planes. On the other hand, for sample Yb-Fe0.6, a HRTEM image of a $YbFeO_3$ crystal observed through a [110] zone axis is displayed in Fig. 4 c., with spots forming 90° and 59° with respect to the {002} (3.8 Å), corresponding to {2–20} and {2–22} crystal reflections (2.7 and 3.8 Å respectively).

On the other hand, the abundance of this ytterbium ferrite phase drastically drops in sample Yb-Fe0.05, agreeing with our previous XRD results. Thus, the most frequent phase present in sample Yb-Fe0.05 is an iron oxide phase (Fe_3O_4, γ-Fe_2O_3 or even a solid solution between both phases), as displayed in Fig. 4e. In the DDP included in this figure, diffraction spots, which may be attributed to Fe_3O_4 oriented along a [110] zone axis, are observed, particularly {311}-type and {-2-22} crystal reflections, whose distances are 2.7 and 2.6 Å forming 63° and 58° angles respectively. Therefore, only a small fraction of $YbFeO_3$ might be formed during the synthesis of sample Yb-Fe0.05 due to the low concentration of Yb in the hydrothermal reaction mixture. In this case, these iron oxide NPs showed very homogeneous size and they expose very clear surface facets. Some evidences of the formation of very small amounts of iron oxides were found in all samples with the exception of Yb-Fe2, in which the amount of ytterbium is appropriate to consume all the added iron to form the mixed oxide. The glycol used as a solvent in the reaction could reduce the Fe^{3+}, leading to the formation of magnetite. However, the hexanediamine added as surfactant also prevents this reduction reaction by the coordination ability of the amine group.

Fig. 5 summarizes the most remarkable results on NP chemical characterization via EDX spectroscopy. The application of this technique to the five samples analyzed (Fig. 5), sheds information on the distribution of iron and ytterbium in the NPs. This figure displays the HAADF-STEM images of each sample on the first column, as well as compositional maps for iron, ytterbium and the mixture of these two elements, and EDX spectra collected for the same region shown in the HAADF-STEM images, in the following columns. EDX maps show a homogeneous distribution of iron and ytterbium in the NPs from Yb-Fe2 and Yb-Fe1 samples as neither green nor red colored regions are visible in the Fe + Yb map, either within NPs or among crystallites (Fig. 5a and 5 b). Nevertheless, greenish and reddish crystals are quite noticeable in these Fe + Yb EDX maps for Yb-Fe0.6 and Yb-Fe0.3 samples (Fig. 5c and 5 d), which suggests the presence of heterogeneities in Yb and Fe composition between NPs. However, no color variations are observed within each crystal, which may indicate that the inner composition of each nanoparticle in these samples is quite homogeneous. On the other hand, the presence of Yb in Yb-Fe0.05 is relatively scarce, as depicted in Fig. 5 e, although well distributed among all NPs. Thus, NPs are mainly formed by iron oxides containing scarce Yb-based phases, which agrees with our previous XRD and TEM results.

Additionally, EDX spectra for all the samples, located on the last column of Fig. 5, reveal X-ray peaks associated to both elements, iron and ytterbium. Quantification obtained from the analyses of these EDX spectra are shown in Table 3 Notice that the Fe:Yb ratio in the samples mainly formed by $YbFeO_3$ NPs (Yb-Fe2, Yb-Fe1, Yb-Fe0.6, and Yb-Fe0.3) is almost 1.1, meaning that there is a similar fraction of ytterbium and iron. Therefore, this directly corresponds to the stoichiometry of the mixed oxide, o-$YbFeO_3$. Hence, these results corroborate the preferential formation of the mixed oxide in all samples in which the ytterbium concentration is high enough to form this compound. On the other hand, the quantitative results from sample Yb-Fe0.05 confirm, as expected, the negligible amount of Yb present in these nanoparticles.

3.2. *Effect of degree of autoclave filling and autogenous pressure*

In order to study the influence of conditions needed to reach the critical temperature value during the solvothermal reaction, the filling level of the reactor has been changed, as previously explained. We have studied the characteristics of NPs obtained working at lower autogenous pressure values.

Fig. 6 displays DRX powder diffractograms of YbFeO3 NPs samples synthesized by using an autoclave filling volumes of 66%, but varying the molar Fe/Yb precursor's ratios from 1 to 2. In addition, Table S.II (supplementary information) shows the experimental values of the recorded XRD peaks, 2θ degrees with the corresponding Miller indices (hkl) indexation. The percentages of each of the mineral phases present in these samples, calculated by using DIFFRAC.EVA.V3.0 software, are summarized in Table 2. It has been found that there is a majority of peaks related to an orthorhombic $YbFeO_3$ phase [44], with a series of additional small broad peaks, which may be attributed either to a hexagonal YbFeO3 phase [45], or a trigonal YbFe2O4 phase [44]; suggesting the presence of a fraction of these additional ytterbium ferrite phases, either as small NPs or included as small crystal inside the orthorhombic $YbFeO_3$ NPs. Is important to note that, several of these peaks can also be attributed to a cubic (space group Fd-3m) iron oxide phase (either Fe_3O_4 (International Centre for Diffraction Data. Powder Diffraction FileTM (PDF®) 2018–2019, file JCPDS 89–0691. Http://www.icdd.com: 2018) or γ-Fe_2O_3 [46]. This seems to suggest the presence of a small population of NPs of an iron oxide phase origin in both samples. Moreover, three well-defined peaks are observed, which can be related to an intermediate rhombohedral (space group R-3m) YbOCl phase (International Centre for Diffraction Data. Powder Diffraction FileTM (PDF®) 2003, file JCPDS 49–1802. http://www.icdd.com). The presence of this phase formed as an intermediate of the reaction, indicates the lower efficiency of these synthesis conditions to form hybrid NPs.

Quantification of EDX results for these two samples are contained in

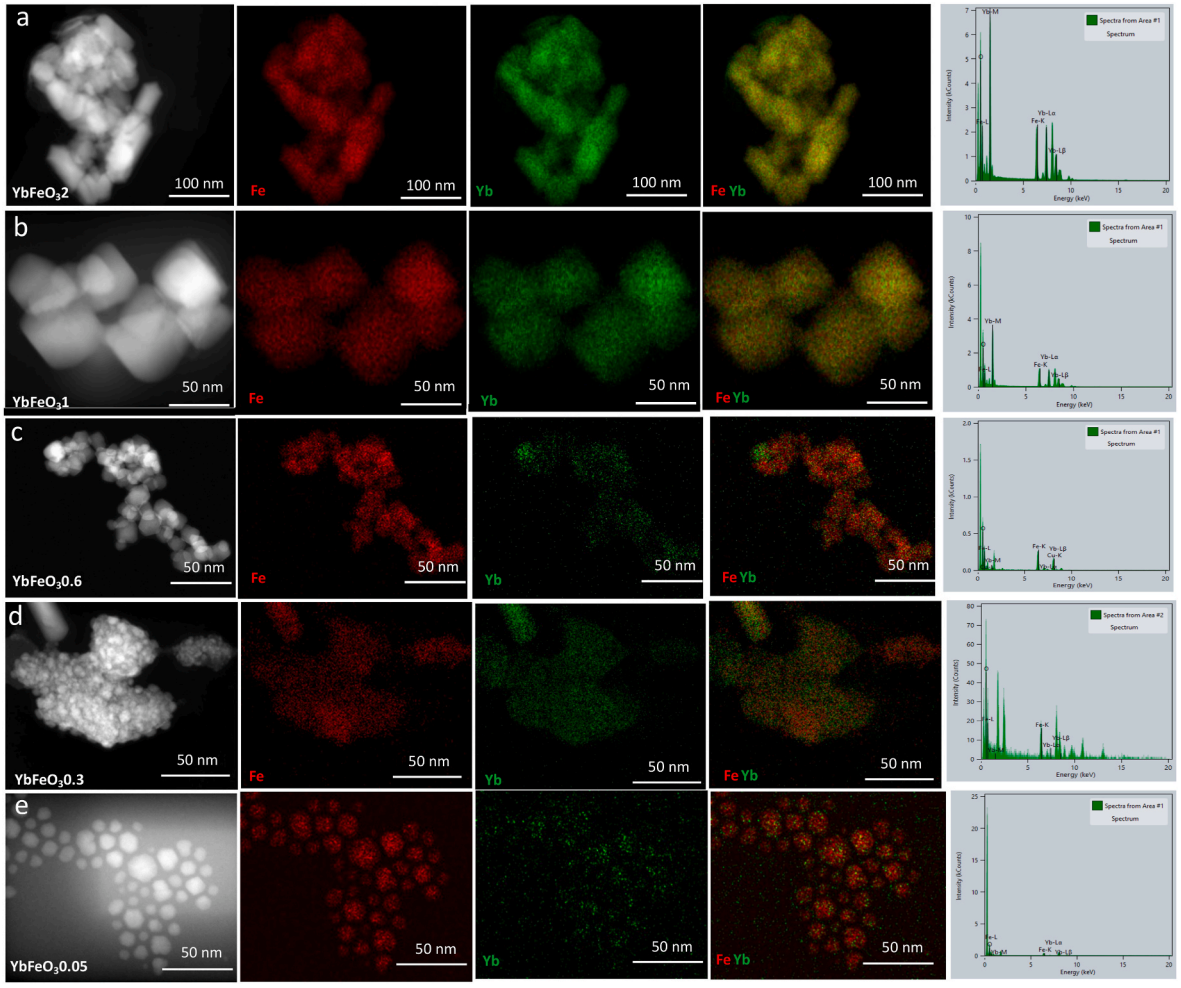

Fig. 5. HAADF-STEM images and EDX analyses of Yb–Fe samples. Each row in the figure corresponds to a sample: Yb-Fe2_80 (a), Yb-Fe1_80 (b), Yb-Fe0.6_80 (c), Yb-Fe0.3_80 (d), and Yb-Fe0.05_80 (e). HAADF-STEM images of each of these samples are located on the first column, while Fe, Yb, and Fe + Yb EDX chemical maps are on the following ones. The last column corresponds to EDX spectra acquired on the same region depicted in the previous HAADF-STEM images located on the first column of the figure.

Table 3
Iron and ytterbium quantification obtained from the analyses of EDX spectra.

NPs	Iron Atomic Fraction (%)	Ytterbium Atomic Fraction (%)
Yb-Fe2	54	46
Yb-Fe1	55	45
Yb-Fe0.6	53	47
Yb-Fe0.3	55	45
Yb-Fe0.05	99	1
Yb–Fe2L	52.6	47.4
Yb–Fe1L	54.3	44.6

Table 3. As in the case of NPs prepared at higher autogenous pressure, they possess an atomic iron and ytterbium ratio very close to 1. Therefore, as no significant differences in iron and ytterbium percentages in the final NPs are obtained, this indicates that doubling the starting ytterbium precursor concentration does not affect the final proportion of Yb inside the NPs.

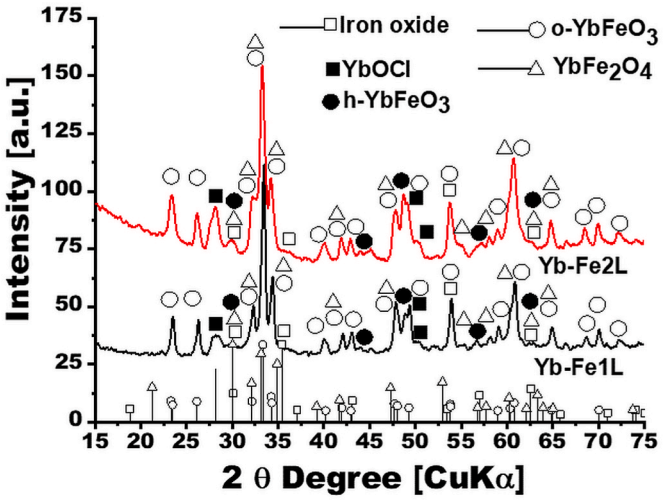

Fig. 6. XRD powder diffractograms recorded for Yb–Fe NPs samples synthesized with a 60% autoclave filling volume and changing the starting ytterbium/iron molar precursor ratio.

3.3. Functionalization

The aim of this work is to obtain biocompatible NPs with appropriate characteristics to be used as CA for medical imaging. For this purpose, it is necessary to develop a proper functionalization process that provides

biocompatibility, allows further crosslinking with other biomolecules, and decreases NP aggregation. Hexanediamine as capping agent has been introduced in situ in the solvothermal reaction. This compound is used as surfactant to control NP formation and growth at the high temperature used during the solvothermal process. However, in order to obtain biocompatible and hydrophilic NPs, the hexanediamine ligand is exchanged by a biocompatible and hydrophilic molecule. As we have previously indicated, the tripeptide GSH is used for this purpose due to its biocompatibility and the availability of several free terminal functional groups susceptible for subsequent crosslinking. Taking into account the results obtained from compositional and structural characterization, NPs prepared at high degree of autoclave filling have been selected to be functionalized, given that these synthesis conditions lead to a higher reaction yield. A general view of functionalized GSH-Yb-Fe1 and GSH-Yb-Fe2 can be observed in the TEM micrograph in Fig. 7a and 7 b, respectively. Although GSH-Yb-1 NPs maintain their previous circle assembly conformation, both functionalized GSH-NPs show a lower aggregation than non-functionalized NPs (Fig. 3b and 3 a respectively), probably due to a decrease in inter-particle interactions. Fig. 7c and 7 d shows NP size distribution, fitted to Gaussian functions, for GSH- Yb-Fe1 and Yb-Fe2, respectively. Functionalized NPs present narrower and more homogeneous size distribution than the same NPs before functionalization, indicating the efficiency of the functionalization process. Additionally, an important decrease of the average size is observed in both cases, in spite of the functionalization being performed after NP synthesis. Considering that the functionalization is carried out by overnight incubation of NPs with a GSH concentrated solution, the molecules probably link to the NP surface increasing its colloidal stability and consequently decreasing the aggregation between particles. This leads to a lower average size and narrower size distribution for functionalized NPs.

DLS experiments have been performed with the aim to analyze the change in colloidal stability in functionalized NPs. Naked NPs present extremely large hydrodynamic size, specifically 820 ± 120 nm for Yb-Fe1 and 738 ± 221 nm for Yb-Fe2, indicating low colloidal stability and a tendency to aggregate in solution. Nevertheless, an important decrease in these hydrodynamic values is obtained for functionalized NPs (190 ± 21 nm for GSH-Yb-Fe1 and 184 ± 18 nm for GSH-Yb-Fe2), with PDI values lower than 0.2. Thus the GSH functionalization process induces an increase in colloidal stability that is crucial for biomedical applications.

Fig. 8 summarizes the most remarkable results on the chemical characterization of functionalized GSH-NPs via EDX spectrometry. This technique not only sheds information on the ytterbium and iron distribution, but also allows to check the functionalization process by studying the sulfur map coming from GSH. The application of this technique to GSH-Yb-Fe1 (Fig. 8a to 8 f) and GSH-Yb-Fe2 (Fig. 8g to 8 l) show that the composition of the NPs is as expected. EDX spectra for both samples, such as the one presented in Fig. 8g and 8 l, reveal X-ray peaks associated to both materials forming the NP (Fe and Yb) and also to sulfur (S), which Kα-peak appears at 2.31 keV. This last element indicates the presence of the GSH molecule. The GSH molecule is composed by carbon, oxygen, nitrogen, hydrogen and sulfur due to a thiol group present in the cysteine, one of the three amino acids present in GSH. Note that other expected peaks, such as the ones for carbon and oxygen, are also present in the spectra. Nevertheless, the signals corresponding to the nanoparticles are screened by the ones corresponding to the carbon support and by organic residual particles possibly present in the electron microscopy grid. In this sense, the copper signal visible in all spectra is produced by the copper in the grid. Observing the EDX maps, we can conclude that the NPs are in all the cases, totally covered with S. The S-map highly agrees with the map of the majority element in each type of NP. As expected, the quantification of sulfur in the NPs rises low percentages of this element in comparison to iron or ytterbium. There is only a S atom in each GSH molecule linked to the NP surface, versus a 30 nm core composed by $FeYbO_3$. These results indicate that the GSH has been linked to the NPs surface functionalizing them. However, in order to deepen in the functionalization mechanism and find which GSH functional group (amine, carboxyl or thiol) is linked to the NP, Fourier Transform Infrared Spectroscopy (FTIR) spectra of free GSH and GSH-Yb-Fe1, are shown in Fig. 9. Basically, the free GSH spectrum shows a peak at 3350 cm^{-1}, characteristic of the $–NH_2$ group, the peak at 2530 cm^{-1} due to S–H stretching group and a peak at 1600 cm^{-1} representative of the –COOH stretching. Interestingly, the peak at 2530 cm^{-1} corresponding to the S–H stretching vibration of GSH, disappears in the GSH- Yb-Fe1_80 NPs, which indicates that GSH molecules anchored on the surface of NP through –S bonding.

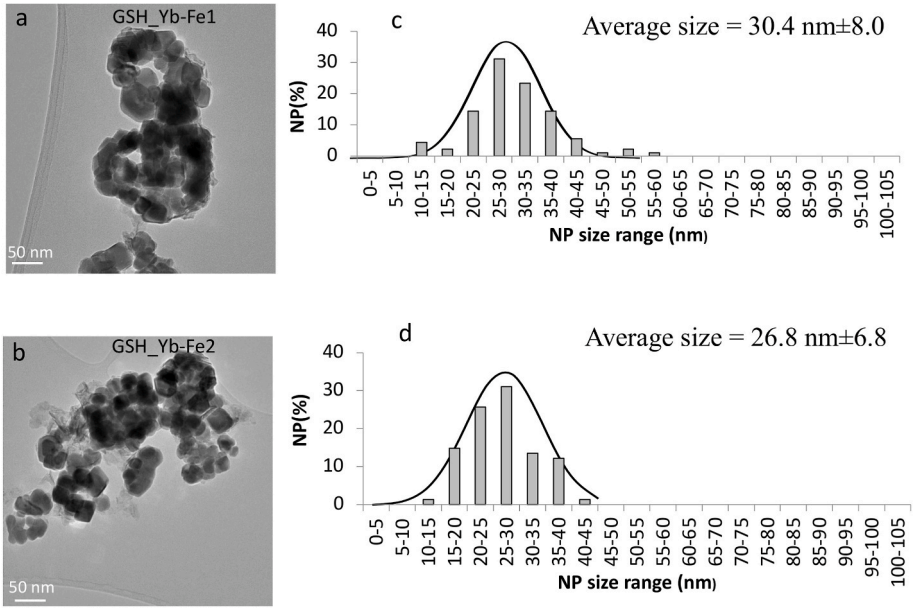

Fig. 7. TEM micrographs for: GSH- Yb-Fe1_80 functionalized NPs (a), for GSH- Yb-Fe2_80 functionalized NPs, and their corresponding NP size distribution (c) and (d), respectively.

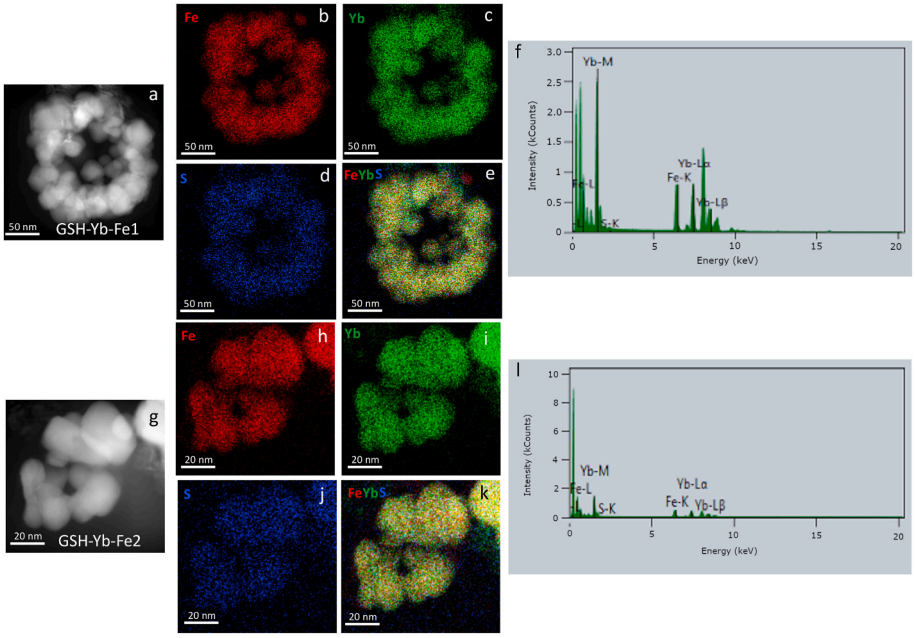

Fig. 8. EDX analyses of functionalized Yb–Fe NPs. HAADF-STEM image (a), EDX maps for Fe (b), Yb (c), S (d) and Fe + Yb + S (e), and EDX spectrum (f) of GSH-Yb-Fe1_80 NPs. HAADF-STEM image (g), EDX maps for Fe (h), Yb (i), S (j) and Fe + Yb + S (k), and EDX spectrum (l) of GSH-Yb-Fe2_80 NPs.

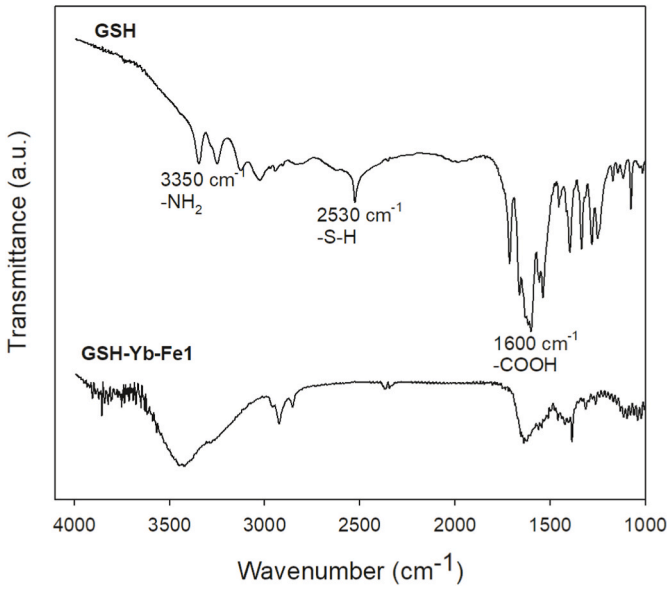

Fig. 9. FTIR spectra obtained for free GSH (a) and GSH-Yb-Fe1 (b).

3.4. X-ray absorption and optical properties

In order to explore the capacity of as synthesized Yb–Fe NPs to be potentially used in medicine as multiplatform CAs in medical imaging by MRI and CT, the magnetic properties and X-ray absorption capacity of the synthesized NPs have been evaluated. On the one hand, Fig. 10 a displays a CT image of a cylindrical preforms sample consisting on pressed dried Yb-Fe1 NPs powder. In this image, the white regions correspond to areas where the X-rays completely pass through the sample, while the grey/black regions correspond to areas where the X-rays are partially or totally attenuated. Similarly, the red line represents an intensity profile of the X-rays recorded by the detector located behind the sample. From this image, a sharp decrease in the intensity line of the X-rays recorded by the X-ray detector has been observed, when they pass

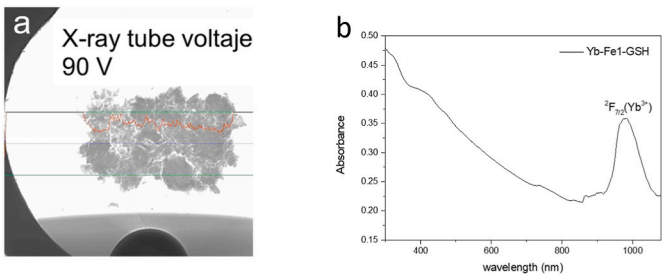

Fig. 10. CT image of a cylindrical preformed sample consisting of pressed dried Yb-Fe-1 NPs powder (a). NIR-Vis absorption spectrum for Yb–Fe1-GSH NPs (b).

through the detection region covered by the preform sample of Yb-Fe-1 NPs, as a consequence of the absorption of 83% of the initial intensity of the incident X-rays. This result demonstrates the potential capacity of these ytterbium ferrite NPs to be used in the manufacture of CTs for X-ray medical imaging techniques. Fig. 10 b shows the absorption spectrum in the NIR-Vis spectral range for Yb–Fe1-GSH. The absorption spectrum displays a main absorption band located at 850–1100 nm centered at 978 nm, that can be attributed to the spin-allowed $^2F_{7/2} \rightarrow {}^2F_{5/2}$ transition of Yb^{3+}, as reported in previous works [30,47].

On the other hand, although the magnetic behavior of these nanoparticles will be the topic of a future study, we have added a small preliminary discussion in the supplementary material.

3.5. Biocompatibility and medical image potential applications

3.5.1. Cytotoxicity

As previously indicated, one key property of these NPs regarding medical applications, is their cytotoxicity, which can initially be studied through cytotoxicity assays. MTT cell viability assays for Jurkat cells incubated with the different NPs are presented in Fig. 11 a (for NP concentrations of 1,5 μg/ml) and 11.b (for 15 μg/ml). These graphics present the percentage of viability for the incubated Jurkat cells without the presence of NPs (NP(-)) or incubated with Yb-Fe1 and with GSH- Yb-Fe1. Each experiment has been performed, independently by triplicate. Graphics in Fig. 11 show mean (bars) and standard deviation of the

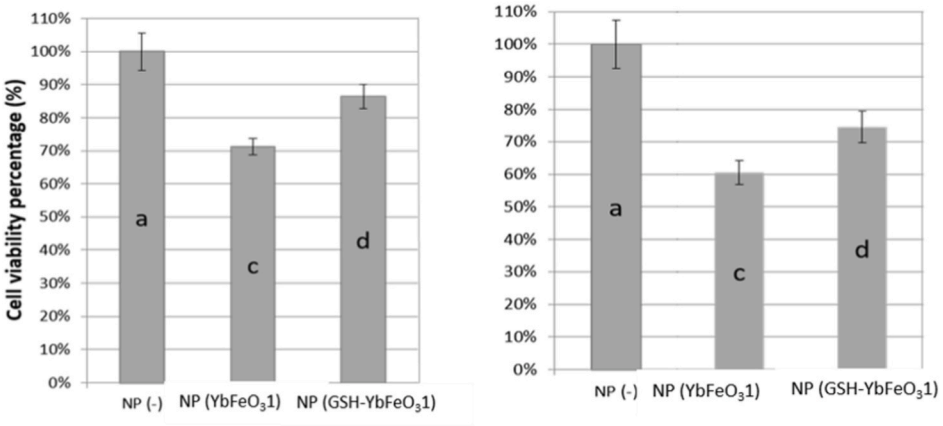

Fig. 11. MTT Cell Viability assay of Jurkat tumor cells incubated with the indicated type of NP, in the presence of NP concentrations of 1.5 μg/ml (a) or 15 μg/ml (b). Viability of cells cultured in the presence of 10% dimethyl sulfoxide (DMSO) is 8.79%.

percentage of viable cells (considering viability of cells cultured in the absence of NP as 100% viable). Similar letters in the columns indicate no statistical difference. Different letters indicate significance difference with a confidence level of 95%.

This work shows for the first time, GSH hybrid ytterbium iron oxide NPs. Although few results about cytotoxicity of ytterbium/iron oxide NPs have been reported, some works present results about biocompatibility for different hybrid NPs containing ytterbium, showing a dose dependency for cytotoxicity, as well as an increase of cell viability when NPs are functionalized [48,49]. The most remarkable results that we can observe from these experiments is the higher cell viability obtained for functionalized NPs. Viability of cells cultured in the presence of naked Yb-Fe1 are 71% and 60% for NP concentration of 1.5 and 15 μg/ml, respectively. However, in the case of GSH-. Yb-$F_3$1 NPs, the percentage of viable cells in the presence of 1,5 μg/ml NPs (the most common concentration used in the literature for these experiments), is 87% (Fig. 11a), indicating the considerably low cytotoxicity of these NPs. For GSH functionalized NPs even when we use concentrations as high as 15 μg/ml (Fig. 11b), we still find cell viability percentages up to 75%. These results indicate that the toxicity profile of functionalized NPs is favorable for *in vivo* applications. Differences in cell viability found between naked and functionalized NPs confirm that the NPs have been properly functionalized and that the GSH functionalization process provides NPs with biocompatible features.

3.5.2. Medical image potential applications

CT and MRI images of Yb-Fe1 NPs at different concentrations in phantoms have been studied, and results obtained from these experiments are shown in Fig. 12. The CT images obtain at different NP concentrations are displayed in Fig. 12 a; and the corresponding X-ray attenuation (CT) intensity values as a function of concentration, are represented in Fig. 12 b. As expected, CT signal of these hybrid NPs increases with Yb concentration, reaching relatively high values. For low Yb concentration, there is no significant increase in CT contrast, however, the signal intensity considerably rises for higher NP concentration. We have also evaluated the contrast capability of Yb-Fe1 NPs for *T2* weighted MRI, at different Fe concentrations [50]. Fig. 12 c shows the *T2* modal MRI images of Yb-Fe1 NPs for different Fe concentrations. The signal enhancement extremely increases even for the lowest NP concentrations, indicating the potential of Yb-Fe1 NPs as powerful negative *T2* MRI contrast agent [51].

4. Conclusions

A novel method to prepare functionalized and biocompatible GSH-Yb-Fe NPs by solvothermal reaction has been developed. We have demonstrated that GSH molecules properly link to the NP surface by the thiol group, keeping the carboxylic and amine GSH functional groups available for subsequent bioconjugations. NPs functionalized with GSH present higher colloidal stability and lower hydrodynamic sizes than naked NPs, decreasing the aggregation level.

The ytterbium/iron ratio used as precursors has a clear influence on NP size average. Bigger NPs are found for higher ytterbium/iron ratios, probably due to the decrease of nucleation frequency induced by the chloride ions introduced in the ytterbium precursor compound (ytterbium chloride), together with the size increase by Ostwald ripening when the amount of ytterbium ions in the reaction media is sufficient for saturation. In all cases, mixed oxide NPs show homogeneous ytterbium/

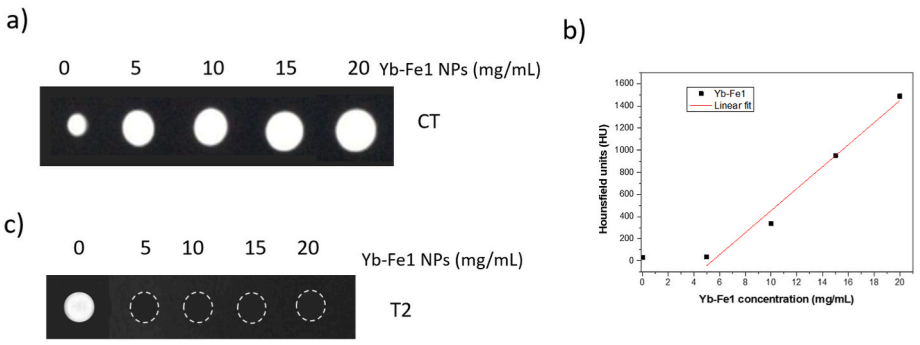

Fig. 12. CT images of Yb-Fe1 NPs at different concentrations (a). CT signal intensity of Yb-Fe1 NPs plotted against the concentration (symbols). The linear fit (red line), has been performed excluding the signal intensity when NPs concentration is zero. (b). The T2 -weighted MR images of Yb-Fe1 NPs at different concentrations (c). (For interpretation of the references to color in this figure legend, the reader is referred to the Web version of this article.)

iron distribution, with similar percentages of iron and ytterbium, indicating formation of $YbFeO_3$ NPs with the 1:1 stoichiometry.

Cuboctahedral NPs are formed for high ytterbium/iron ratios, but only when the degree of reactor filling is 80% or higher. Under these conditions, lower times to reach the critical temperature values, together with high precursor concentrations induce a fast nucleation. Cylindrical Yb–Fe oxide nanorods are obtained when the solvothermal reaction is carried out at a lower degree of reactor filling. Under these conditions, longer time and higher temperatures are necessary to reach the solvothermal reaction, decreasing the saturation and consequently the nucleation rate. Consequently, these conditions lead to the formation of YbOCl as intermediate, decreasing the reaction yield.

The developed NPs show a high biocompatibility with low cytotoxicity that clearly decreases when NPs are functionalized with GSH. Additionally, NPs show good MRI/CT imaging ability, thereby indicating promising potential as a dual MRI/CT contrast agent.

Funding

This work was supported by the Spanish Ministry of Economy and Competitiveness (MAT2015-67354-R) for O.B-M and PID2020-117544RB-I00, for F.G-CPECART-0096-2020, Consejería Salud y Familias. JA Spain; and P20_01293, Consejería Economía, Conocimiento, Empresas y Universidad. JA Spain; for F.G-C; Spanish MCIN/AEI/ 10.13039/501100011033 (project PID2020-118329RB-I00) for E.N; and MINECO/ FEDER Project MAT2017-87579-R.

Declaration of competing interest

The authors declare that they have no known competing financial interests or personal relationships that could have appeared to influence the work reported in this paper.

Acknowledgments

The authors would like to thank the Nanotechnology in translational hyperthermia RED2018-102626-T network.

Appendix A. Supplementary data

Supplementary data to this article can be found online at https://doi.org/10.1016/j.ceramint.2022.06.194.

References

[1] G. Hashimoto, M. Fukui, P. Sorajja, J.L. Cavalcante, Essential roles for CT and MRI in timing of therapy in tricuspid regurgitation, Prog. Cardiovasc. Dis. 62 (2020) 459–462.
[2] B.C. Baljer, S. Kolhe, C.D. Chan, F. Nicoli, A. Ghanbasha, M.J. Brookes, Z. Gamie, K. M. Ghosh, T.B. Beckingsale, D.B. Saleh, M. Ragbir, C.H. Gerrand, L. Jeys, J. C. Knight, G. Petrides, K.S. Rankin, Advances in image enhancement for sarcoma surgery, Cancer Lett. 483 (2020) 1–11.
[3] N. MacRitchie, M. Frleta-Gilchrist, A. Sugiyama, T. Lawton, I.B. McInnes, P. Maffia, Molecular imaging of inflammation - current and emerging technologies for diagnosis and treatment, Pharmacol. Ther. (2020) 211.
[4] K. Khan, S. Cascinu, D. Cunningham, S.-Y. Kim, E. Oki, T. Seery, L. Shen, S. Siena, C. Tournigand, N.S. Turhal, A. Hendlisz, Imaging and clinical correlates with regorafenib in metastatic colorectal cancer, Cancer Treat Rev. 86 (2020).
[5] Z. Du, A. Gupta, C. Clarke, M. Cappadona, D. Clases, D. Liu, Z. Yang, S. Karan, W. Price, X. Xu, Porous upconversion nanostructures as bimodal biomedical imaging contrast agents, J. Phys. Chem. C 124 (2020) 12168–12174.
[6] D. Saslow, C. Boetes, W. Burke, S. Harms, M.O. Leach, C.D. Lehman, E. Morris, E. Pisano, M. Schnall, S. Sener, R.A. Smith, E. Warner, M. Yaffe, K.S. Andrews, C. A. Russell, American Cancer Society guidelines for breast screening with MRI as an adjunct to mammography, Ca-a Cancer J. Clin. 57 (2007) 75–89.
[7] R. Fusco, N. Raiano, C. Raiano, F. Maio, P. Vallone, M.M. Raso, S.V. Setola, V. Granata, M.R. Rubulotta, M.L. Barretta, T. Petrosino, A. Petrillo, Evaluation of average glandular dose and investigation of the relationship with compressed breast thickness in dual energy contrast enhanced digital mammography and digital breast tomosynthesis, Eur. J. Radiol. 126 (2020).
[8] S.H. Heywang-Koebrunner, A. Hacker, S. Sedlacek, Magnetic resonance imaging: the evolution of breast imaging, Breast 22 (2013) S77–S82.
[9] S.T. Cochran, Anaphylactoid reactions to radiocontrast media, Curr. Allergy Asthma Rep. 5 (2005) 28–31.
[10] M. Mirzaei, M.E. Akbari, M.A. Mohagheghi, S.A.M. Ziaee, M. Mohseni, A novel biocompatible nanoprobe based on lipoproteins for breast cancer cell imaging, Nanomed J. 7 (2020) 73–79.
[11] Y. Ren, S. He, L. Huttad, M.-S. Chua, S.K. So, Q. Guo, Z. Cheng, An NIR-II/MR dual modal nanoprobe for liver cancer imaging, Nanoscale 12 (2020) 11510–11517.
[12] A. Lahooti, S. Sarkar, S. Laurent, S. Shanehsazzadeh, Dual nano-sized contrast agents in PET/MRI: a systematic review, Contrast Media Mol. Imaging 11 (2016) 428–447.
[13] A. Sobczak-Kupiec, J. Venkatesan, A.A. AlAnezi, D. Walczyk, A. Farooqi, D. Malina, S.H. Hosseini, B. Tyliszczak, Magnetic nanomaterials and sensors for biological detection, Nanomed. Nanotechnol. Biol. Med. 12 (2016) 2459–2473.
[14] E. Forte, D. Fiorenza, E. Torino, A.C. di Polidoro, C. Cavaliere, P.A. Netti, M. Salvatore, M. Aiello, Radiolabeled PET/MRI nanoparticles for tumor imaging, J. Clin. Med. 9 (2020).
[15] R. Luo, L. Chen, Q. Li, J. Zhou, L. Mei, Z. Ning, Y. Zhao, M. Liu, X. Lai, J. Bi, W. Yin, D. Gao, Bi3+-Doped BaYF5:Yb,Er upconversion nanoparticles with enhanced luminescence and application case for X-ray computed tomography imaging, Inorganic chem. 59 (2020) 17906–17915.
[16] R.-H. Li, X.-Y. Feng, J. Zhou, F. Yi, Z.-Q. Zhou, D. Men, Y. Sun, Rhomboidal Pt(II) metallacycle-based hybrid viral nanoparticles for cell imaging, Inorganic chem. 60 (2021) 431–437.
[17] L.H. Reddy, J.L. Arias, J. Nicolas, P. Couvreur, Magnetic nanoparticles: design and characterization, toxicity and biocompatibility, pharmaceutical and biomedical applications, Chem. Rev. 112 (2012) 5818–5878.
[18] J.J. Beato-Lopez, M. Dominguez, M. Ramirez-del-Solar, R. Litran, Glutathione-magnetite nanoparticles: synthesis and physical characterization for application as MRI contrast agent, SN Appl. Sci. 2 (2020).
[19] S. Laurent, D. Forge, M. Port, A. Roch, C. Robic, L.V. Elst, R.N. Muller, Magnetic iron oxide nanoparticles: synthesis, stabilization, vectorization, physicochemical characterizations, and biological applications (vol 108, pg 2064, 2008), Chem. Rev. 110 (2010), 2574-2574.
[20] D.L. Huber, Synthesis, properties, and applications of iron nanoparticles, Small 1 (2005) 482–501.
[21] M. Bouche, J.C. Hsu, Y.C. Dong, J. Kim, K. Taing, D.P. Cormode, Recent advances in molecular imaging with gold nanoparticles, Bioconjugate Chem. 31 (2020) 303–314.
[22] A. Ghazanfari, S. Marasini, X. Miao, J.A. Park, K.-H. Jung, M.Y. Ahmad, H. Yue, S. L. Ho, S. Liu, Y.J. Jang, K.S. Chae, Y. Chang, G.H. Lee, Synthesis, characterization, and X-ray attenuation properties of polyacrylic acid-coated ultrasmall heavy metal oxide (Bi2O3, Yb2O3, NaTaO3, Dy2O3, and Gd2O3) nanoparticles as potential CT contrast agents, Colloids Surf. A Physicochem. Eng. Asp. 576 (2019) 73–81.
[23] Y. Liu, K. Ai, J. Liu, Q. Yuan, Y. He, L. Lu, A high-performance ytterbium-based nanoparticulate contrast agent for in vivo X-ray computed tomography imaging, Angew. Chem. Int. Ed. 51 (2012) 1437–1442.
[24] C. Zwicker, M. Hering, R. Langer, Computed tomography with iodine-free contrast media, Eur. Radiol. 7 (1997) 1123–1126.
[25] H. Kobayashi, K. Fujiwara, N. Kobayashi, T. Ogawa, M. Sakai, M. Tsujimoto, O. Seri, S. Mori, N. Ikeda, Stability of cluster glass state in nano order sized YbFe2O4 powders, J. Phys. Chem. Solid. 103 (2017) 103–108.
[26] M. Carril, I. Fernandez, J. Rodriguez, I. Garcia, S. Penades, Gold-coated iron oxide glyconanoparticles for MRI, CT, and US multimodal imaging, Part. Part. Syst. Char. 31 (2014) 81–87.
[27] T. Nishimura, S. Hosokawa, Y. Masuda, K. Wada, M. Inoue, Synthesis of metastable rare-earth-iron mixed oxide with the hexagonal crystal structure, J. Solid State Chem. 197 (2013) 402–407.
[28] J. Zhang, K. Huang, L. Yuan, S. Feng, Mineralizer effect on facet-controllable hydrothermal crystallization of perovskite structure YbFeO3 crystals, CrystEngComm 20 (2018) 470–476.
[29] S. Yamini, M. Gunaseelan, G.A. Kumar, S. Singh, G.C. Dannangoda, K. S. Martirosyan, D.K. Sardar, S. Sivakumar, A. Girigoswami, J. Senthilselvan, NaGdF4:Yb,Er-Ag nanowire hybrid nanocomposite for multifunctional upconversion emission, optical imaging, MRI and CT imaging applications, Microchim. Acta 187 (2020).
[30] K. Halubek-Gluchowska, D. Szymanski, T.N.L. Tran, M. Ferrari, A. Lukowiak, Upconversion luminescence of silica-calcia nanoparticles Co-doped with Tm3+ and Yb3+ ions, Materials 14 (2021).
[31] AM Abu-Dief, AAH Abdel-Mawgoud, Functionalization of magnetic nanoparticles for drug delivery, SF J Nanochem. Nanotechnol. 1 (1) (2018) 1005, 6.
[32] M. Shringirishi, S.K. Prajapati, A. Mahor, S. Alok, P. Yadav, A. Verma, Gold nanoparticles: promising and potential nanomaterial, Int. J. Pharmaceut. Sci. Res. 4 (2013) 4068–4082.
[33] M.S. Saddik, M.M.A. Elsayed, M.S.A. Abdelkader, M.A. El-Mokhtar, J.A. Abdel-Aleem, A.M. Abu-Dief, M.E. Al-Hakkani, H.S. Farghaly, H.A. Abou-Taleb, Novel green biosynthesis of 5-fluorouracil chromium nanoparticles using harpullia pendula extract for treatment of colorectal cancer, Pharmaceutics 13 (2021).
[34] C. Fernández-Ponce, J.M. Mánuel, R. Fernández-Cisnal, E. Félix, J.J. Beato-Lopez, J.P. Muñoz-Miranda, A.M. Beltrán, A.J. Santos, F.M. Morales, M.P. Yeste, O. Bomati-Miguel, R. Litran, F. García-Cózar, Superficial characteristics and functionalization effectiveness of non-toxic glutathione-capped magnetic, fluorescent, me-tallic and hybrid nanoparticles for biomedical applications, Metals 11 (2021) 24.
[35] S. Hosokawa, S. Iwamoto, M. Inoue, Synthesis of mesoporous needle-shaped ytterbium oxide crystals by solvothermal treatment of ytterbium chloride, J. Am. Ceram. Soc. 90 (2007) 1215–1221.

[36] S. Hosokawa, H.-J. Jeon, S. Iwamoto, M. Inoue, Synthesis of rare earth iron-mixed oxide nanoparticles by solvothermal methods, J. Am. Ceram. Soc. 92 (2009) 2847–2853.
[37] J.J. Beato-Lopez, M.L. Espinazo, C. Fernandez-Ponce, E. Blanco, M. Ramirez-del-Solar, M. Dominguez, E. Garcia-Cozar, R. Litran, CdTe quantum dots linked to Glutathione as a bridge for protein crosslinking, J. Lumin. 187 (2017) 193–200.
[38] J.J. Beato-Lopez, C. Fernandez-Ponce, E. Blanco, C. Barrera-Solano, M. Ramirez-del-Solar, M. Dominguez, F. Garcia-Cozar, R. Litran, Preparation and characterization of fluorescent CdS quantum dots used for the direct detection of GST fusion proteins regular paper, Nanomater. Nanotechnol. 2 (2012).
[39] A.M. Beltran, J.M. Manuel, R. Litran, E. Felix, A.J. Santos, F.M. Morales, O. Bomati-Miguel, (S)TEM structural and compositional nanoanalyses of chemically synthesized glutathione-shelled nanoparticles, Appl. Nanosci. (2020).
[40] A.M. Abu-Dief, A.A. Essawy, A.K. Diab, W.S. Mohamed, Facile synthesis and characterization of novel Gd2O3-CdO binary mixed oxide nanocomposites of highly photocatalytic activity for wastewater remediation under solar illumination, J. Phys. Chem. Solid. 148 (2021).
[41] A.M. Abu-Dief, W.S. Mohamed, alpha-Bi2O3 nanorods: synthesis, characterization and UV-photocatalytic activity, Mater. Res. Express 4 (2017).
[42] W.S. Mohamed, A.M. Abu-Dief, Synthesis, characterization and photocatalysis enhancement of Eu2O3-ZnO mixed oxide nanoparticles, J. Phys. Chem. Solid. 116 (2018) 375–385.
[43] D.T. Vistica, P. Skehan, D. Scudiero, A. Monks, A. Pittman, M.R. Boyd, Tetrazolium-based assays for cellular viability: a critical examination of selected parameters affecting formazan production, Cancer Res. 51 (1991) 2515–2520.
[44] N. Kimizuka, K. Kato, I. Shindo, I. Kawada, T. Katsura, New compounds OF YB3FE4O10 and YB4FE5O13/5O-13, Acta Crystallogr. Sect. B Struct. Sci. 32 (1976) 1620–1621.
[45] S.M. Tikhanova, L.A. Lebedev, K.D. Martinson, M.I. Chebanenko, I.V. Buryanenko, V.G. Semenov, V.N. Nevedomskiy, V.I. Popkov, The synthesis of novel heterojunction h-YbFeO3/o-YbFeO3 photocatalyst with enhanced Fenton-like activity under visible-light, New J. Chem. 45 (2021) 1541–1550.
[46] H. Sadamura, K. Yamashita, N. Nagai, Crystallographic study of cobalt treatment on GAMMA-FE2O3, J. Appl. Phys. 73 (1993) 6731–6733.
[47] E.L. Guryev, A.S. Smyshlyaeva, N.Y. Shilyagina, E.A. Sokolova, S. Shanwar, A. B. Kostyuk, A.V. Lyubeshkin, A.A. Schulga, E.V. Konovalova, Q. Lin, I. Roy, I. V. Balalaeva, S.M. Deyev, A.V. Zvyagin, UCNP-Based photoluminescent nanomedicines for targeted imaging and theranostics of cancer, Molecules 25 (2020).
[48] R.M. Sabio, S.H. Santagneli, M. Gressier, J.M. Almeida Caiut, W.M. Pazin, I.S. Leite, N.M. Inada, R.R. da Silva, S.J. Lima Ribeiro, M.-J. Menu, Luminescent nanohybrids based on silica and silylated Ru(II)-Yb(III) heterobinuclear complex: new tools for biological media analysis, Nanotechnology (2020) 31.
[49] C. Arboleda, S. He, A. Stubelius, A. Almutairi, Tuning upconversion in Nd(III)-sensitized core-shell nanoparticles for excitation with biobenign wavelength, Abstr. Pap. Am. Chem. Soc. (2017) 254.
[50] S. Liang, Q. Zhou, M. Wang, Y. Zhu, Q. Wu, X. Yang, Water-soluble L-cysteine-coated FePt nanoparticles as dual MRI/CT imaging contrast agent for glioma, Int. J. Nanomed. 10 (2015).
[51] G. Wang, W. Gao, X. Zhang, X. Mei, Au nanocage functionalized with ultra-small Fe3O4 nanoparticles for targeting T-1-T-2 dual MRI and CT imaging of tumor, Sci. Rep. 6 (2016).